Tunable Laser Plasma Accelerator based on Longitudinal Density Tailoring

A. J. Gonsalves,[1] K. Nakamura,[1] C. Lin,[1,2] D. Panasenko,[1,*] S. Shiraishi,[1,3] T. Sokollik,[1,4] C. Benedetti,[1] C. B. Schroeder,[1] C. G. R. Geddes,[1] J. van Tilborg,[1] J. Osterhoff,[1,†] E. Esarey,[1] C. Toth,[1] and W. P. Leemans[1,4]

[1] *Lawrence Berkeley National Laboratory, Berkeley, CA 94720, USA*

[2] *Peking University, Beijing, 100871, P. R. China*

[3] *University of Chicago, Chicago, IL, 60637, USA*

[4] *University of California, Berkeley, CA 94720, USA*

(Dated: July 18, 2011)

Laser plasma accelerators (LPAs) [1] have produced high-quality electron beams with GeV energies from centimeter scale devices [2] and are being investigated as hyperspectral femtosecond light sources producing THz to γ-ray radiation [3–5], and as drivers for future high energy colliders [6, 7]. These applications require a high degree of stability, beam quality, and tunability. Here we report on a technique to inject electrons into the accelerating field of a laser-driven plasma wave and coupling of this injector to a lower-density, separately-tunable plasma for further acceleration. The technique relies on a single laser pulse powering a plasma structure with a tailored longitudinal density profile, to produce beams that can be tuned in the range of 100 to 400 MeV with percent level stability, using < 40 TW laser pulses. The resulting device is a simple stand-alone accelerator or the front-end for a multi-stage higher energy accelerator.

Producing high-quality electron beams from an accelerator requires electron injection into the accelerating field to be localized in time and space. For LPAs that rely on homogeneous plasmas driven with single laser pulses, continuous injection can occur when driving large amplitude plasma waves (wakefields), resulting in large energy spread. Lower energy spread can be achieved through termination of injection by operating near the injection threshold or by injecting enough charge to suppress the wake amplitude (i.e., beam loading). Subsequent termination of the accelerating process at dephasing (i.e., when electrons are starting to outrun the accelerating wave) minimizes energy spread. These mechanisms have produced percent-level energy spread beams [2, 8–10], but small changes in parameters can result in large changes in beam quality. As a result, tunability has been limited necessitating the development of a simple, robust and controlled injection technique combined with an independently controllable accelerating stage.

In general, injection of electrons into a plasma wave occurs when the velocity of background electrons approaches the wake phase velocity. Laser-based methods for boosting the electron velocity have been proposed [11, 12] and implemented [13, 14] to achieve tunable electron beams, but require sophisticated alignment and synchronization of the multiple laser pulses. Injection can also be triggered by introducing electrons into the correct phase of the wake through ionization [15], but so far the technique has resulted in broad energy srepad beams with high divergence [16, 17].

A different approach, that relies on a single laser pulse for powering the LPA, is to momentarily slow down the wake phase velocity to facilitate trapping [18]. The control

of the wake phase velocity can be done by tailoring z the non-linear plasma wavelength $\lambda_{\rm p}(z)$ along the longitudinal coordinate, through control of the electron density $n_{\rm e}$ and the laser parameters. Specifically, $\lambda_{\rm p}(z) = \lambda_{\rm p0}(z)F$, where the linear plasma wavelength $\lambda_{\rm p0}(\mu{\rm m}) \approx 3.3 \times 10^{10}/\sqrt{n_{\rm e}({\rm cm}^{-3})}$ and F is a function of the laser parameters: at low intensity ($a_0 < 1$), $F \approx 1$ and when $a_0 \gtrsim 1$, F can be greater than 1. Here a_0 is the normalized laser vector potential $a_0 = 7.3{\times}10^{-19}[\lambda(\mu{\rm m})]^2 I_0({\rm Wcm}^{-2})$, and I_0 is the peak laser intensity of the laser pulse with wavelength λ. The wake phase velocity [1] is approximately $\beta_p \approx \beta_g/(1 + |\zeta|\lambda_{\rm p}^{-1} d\lambda_p/dz)$, where β_g is the laser group velocity, and $|\zeta|$ is the distance behind the laser.

Previously, phase velocity control by using tailored plasma density profiles was experimentally achieved for low energy beams ($<$ 10's of MeV) [19–21]. In this paper we demonstrate phase velocity reduction by combined relativistic intensity and density downramp effects in a sub-millimeter high density plasma, and the subsequent acceleration of the resulting low energy bunches ($< 30\,{\rm MeV}$) to several hundreds of MeV in a closely coupled lower density capillary discharge based structure. By controlling the densities of the two plasma regions and the focal location of the laser pulse, precise control over trapping and acceleration is achieved and high-quality, stable, and tunable electron beams are generated.

Self-focusing can occur when the laser power $P \gtrsim P_{\rm c}$, where $P_{\rm c}(GW) = 17(\lambda_{\rm p0}/\lambda)^2 \propto 1/n_{\rm e}$ is the critical power for relativistic self-focusing. The high density plasma can therefore increase both a_0 and $d\lambda_{\rm p}/dz$, lowering the phase velocity as illustrated in Fig. 1(a). After focus, $da_0/dz < 0$, $d\lambda_{\rm p}/dz < 0$, and injection is terminated, resulting in a highly localized injector. The electrons are then accelerated to several hundred MeV in the integrated plasma channel, powered by the same drive laser pulse, demonstrating post-acceleration similar to that simulated in Ref. 19, 22–24.

The setup is shown in Fig. 1 (c). Laser pulses with peak power of 40 TW and pulse length of 38 fs from a Ti:sapphire laser system were focused onto longitudinally tailored plasma targets. The injector stage, a supersonic gas jet, was operated without capillary over a wide range of parameters (detailed in the methods section), producing beams with energy up to 60 MeV and energy spread (FWHM) ranging between 1 % and 50 %. A typical electron beam from the injector is shown in Fig. 2 (a) for which the laser energy depletion was $\approx 30\,\%$, leaving significant laser energy for driving a wake in a subsequent structure. Electron beams could be produced within the range $0\,{\rm mm} \leq \Delta x_{\rm f} \leq 3.5\,{\rm mm}$ and the maximum charge was

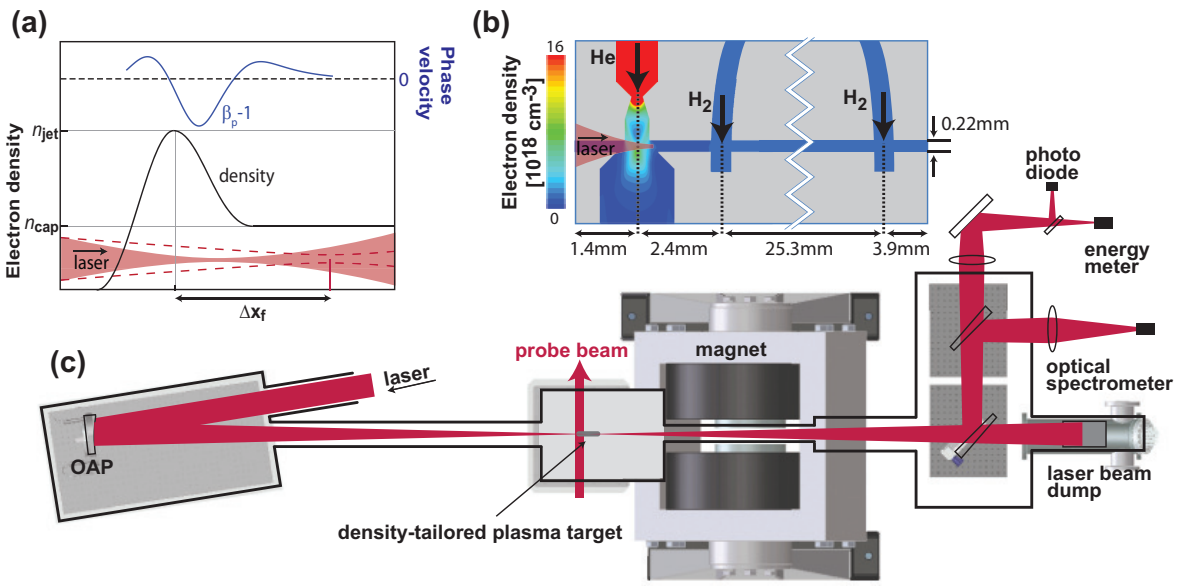

FIG. 1. Experimental layout of the density-tailored laser plasma accelerator. (a) Illustration of the laser focusing onto the plasma target and of the basic physics: The longtudinal on-axis density profile in the region of the gas (black), the location of the vacuum focus with respect to the center of the gas jet Δx_f (red dashed line), the self-focused laser focal position (red shaded area), and the wake phase velocity (blue line). (b) The target schematic and gas profile calculated by a commercial fluid dynamics code, where a supersonic gas jet has been embedded into a capillary which is filled with hydrogen gas. The experimental layout is shown in (c). Pulses from the LOASIS Ti:sapphire laser system of length 38 fs were focused onto the gas targets to a focal spot size of $r_0 = 22\,\mu$m, producing a peak intensity at focus of $4 \times 10^{18}\,\mathrm{Wcm}^{-2}$. The spectra of electron beams emerging from the plasma were obtained using a magnetic spectrometer [25], as described in the methods section. The spectrum and energy of the laser pulses at the capillary output were measured with a spectrometer and pyroelectric energy meter, respectively.

obtained when focusing $\Delta x_\mathrm{f} = 2\,$mm downstream of the jet center. Injection for vacuum focus 3.5 mm downstream of a jet of width $\approx 0.75\,$mm is consistent with the focal location shifting closer to the peak of the density profile due to self-focusing. Phase velocity reduction due to the increase in laser intensity and the decreasing density on the down-ramp of the gas jet resulted in controlled injection.

The gas jet (injector) was then coupled to a lower density plasma produced in a capillary discharge waveguide [26–28] (accelerator). The geometry is shown in Fig. 1 (b). The acceler-

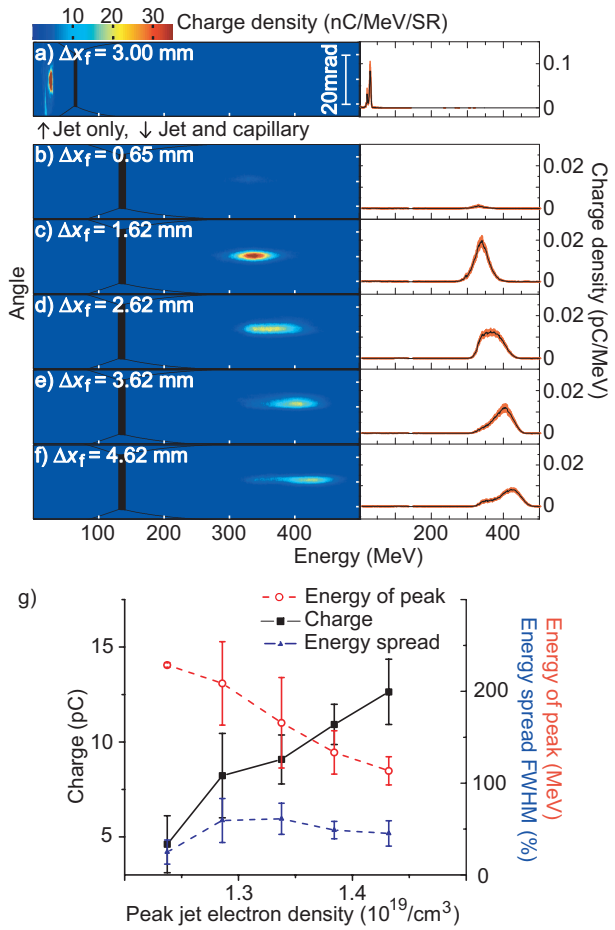

FIG. 2. Electron beam data from both the gas jet and the density-tailored plasma target, demonstrating the post-injection acceleration in the capillary structure and the control over electron beam properties afforded by the density-tailored approach. (a-f) Averaged magnetic spectrometer images from 20 consecutive shots. The black shaded areas in each image represent the regions not covered by the spectrometer cameras. Lineouts of the mean (black curve) and the standard deviation (red area) are on the right of each image. The LPA in (a) comprised only of a helium gas jet with peak electron density $n_{\rm jet} \approx 7 \times 10^{18}\,{\rm cm}^{-3}$ and length (FWHM) 0.75 mm. For (b-f) a helium gas jet with $n_{\rm jet} \approx 7 \times 10^{18}\,{\rm cm}^{-3}$ and length (FWHM) 0.55 mm was coupled to a capillary with density $n_{\rm cap} \approx 1.8 \times 10^{18}\,{\rm cm}^{-3}$ for various focal locations $\Delta x_{\rm f}$. (g) The charge (squares), energy (circles), and energy spread (triangles), as a function of peak jet density for $\Delta x_{\rm f} = 0.62$ mm at capillary density $n_{\rm cap} \approx 1.2 \times 10^{18}\,{\rm cm}^{-3}$. The error bars correspond to the standard deviation of the data.

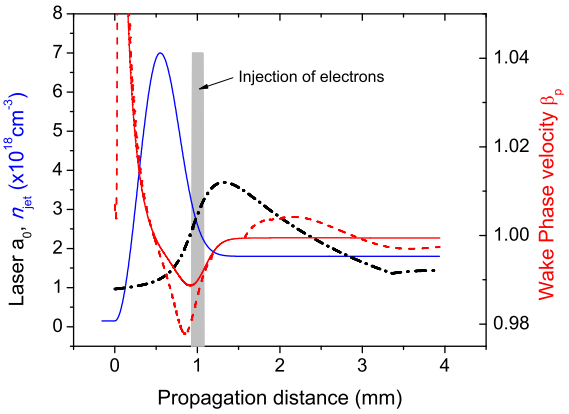

FIG. 3. Simulated evolution of the normalized vector potential a_0 (dash-dot line) as a function of propagation distance for $\Delta x_f = 1.6\,\mathrm{mm}$ and $n_{jet} = 7 \times 10^{18}\,\mathrm{cm}^{-3}$. The blue solid line shows the longitudinal density profile. The phase velocity reduction (red dashed line) was larger than that for the downramp alone (red solid line) due to self-focusing increasing the non-linear plasma wavelength, and trapping of electrons occurred in the grey shaded area. The phase velocities shown are measured in the center of the bubble behind the laser pulse where the longitudinal electric field is 0. The phase velocity reduction at the back of the bubble is approximately a factor of 2 larger.

ator stage was characterized by not injecting gas into the jet nozzle, such that a homogenous hydrogen plasma was formed between the gas slots. No electrons were detected on the magnetic spectrometer for the density range employed ($1 \times 10^{18}\,\mathrm{cm}^{-3} \leq n_{cap} \leq 2.7 \times 10^{18}\,\mathrm{cm}^{-3}$), which is consistent with previous experiments [2]. As evidenced by the shift in the mean of the laser spectral distribution from 803 nm up to 835 nm (caused by transfer of energy from photons to the wake), a significant wakefield was produced in this dark-current-free structure.

When gas was injected into the jet nozzle, high quality beams were observed with energy significantly higher than that with the jet alone. The increase from tens of MeV to hundreds of MeV is consistent with post-acceleration in the lower density structure. The beam properties were controlled by focus location and by jet density. The effect of focus location is shown in Fig. 2 (b-f), where for $n_{jet} \approx 7 \times 10^{18}\,\mathrm{cm}^{-3}$ and $n_{cap} \approx 1.8 \times 10^{18}\,\mathrm{cm}^{-3}$ each image is an average of 20 consecutive electron beams for various Δx_f (cf. Fig. 1 (a)). Also shown are lineouts of each image, with the average denoted by the black line and the standard deviation by the red shaded area. The effect of jet density is shown in Fig. 2 (g), which shows

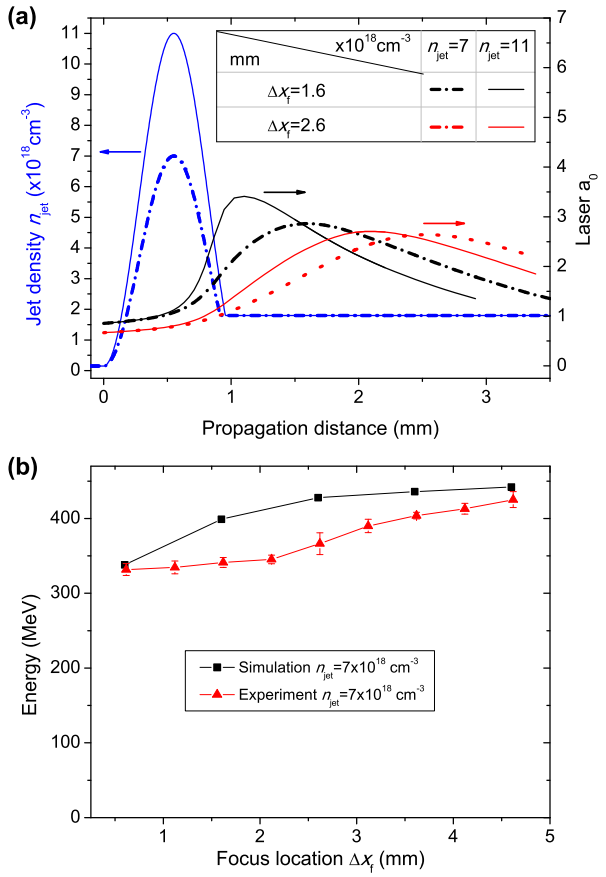

FIG. 4. Comparison of the energy gain observed in simulation and experiment, demonstrating tunability of electron beam energy via control over laser pulse diffraction. (a) Simulated evolution of the normalized vector potential a_0 as a function of propagation distance for different focal locations, $\Delta x_\mathrm{f} = 1.6\,\mathrm{mm}$ (black) and $\Delta x_\mathrm{f} = 2.6\,\mathrm{mm}$ (red), and peak densities, $n_\mathrm{jet} = 7 \times 10^{18}\,\mathrm{cm}^{-3}$ (dotted lines) and $n_\mathrm{jet} = 11 \times 10^{18}\,\mathrm{cm}^{-3}$ (solid lines). The blue lines shows the longitudinal density profile. (b) The energy gain computed as a function of n_jet for different focal locations, along with experimental data for the conditions of Fig. 2 (b-g). The error bars correspond to the standard deviation of the data.

beam energy (red circles), charge (black squares), and energy spread (triangles). The increased bunch charge at higher density is expected due to the slower wake phase velocity and increased laser self-focusing and steepening, all of which enhance trapping. For Fig. 2 (c), which is typical of the performance achieved, the beam energy, energy spread (FWHM), and divergence (FWHM) were 341 MeV, 11 %, and 2.5 mrad, respectively. The production of tunable beams with low energy spread and divergence, and with 100 % injection proba-

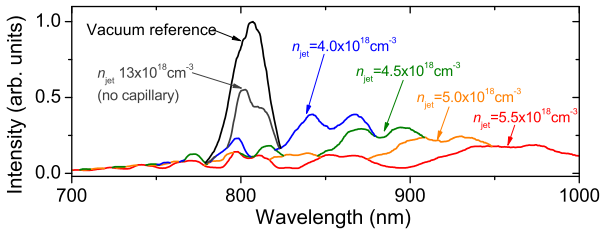

FIG. 5. Laser spectrum for no plasma (black), jet only with density 13 $\times 10^{18}\,\mathrm{cm}^{-3}$ and length (FWHM) 0.75 mm (grey), and jet and capillary with jet length 0.55 mm and density between $4 \times 10^{18}\,\mathrm{cm}^{-3}$ and $5.5 \times 10^{18}\,\mathrm{cm}^{-3}$ (colored plots), each with $n_{\mathrm{cap}} \approx 1.5 \times 10^{18}\,\mathrm{cm}^{-3}$.

bility (which is not observed for conventional self trapping) is consistent with realization of phase-velocity triggered injection and post-acceleration as simulated in Ref. 19, 22–24. The average divergence was 2.2 mrad for the consecutive beams in Fig. 2 (b-f) compared with $5 - 11$ mrad beams produced with other state-of-the-art injection techniques [14, 20].

Energy spread was correlated with charge, with a peak observed for 1 pC for Fig. 2 (b-f) and 10 pC for Fig. 2 (g). This suggests that beam loading is not increasing the energy spread, but that phasing of injected electrons into the lower density structure is not optimized. Additional evidence for this is that the highest quality beams had 1 pC charge and energy spread and divergence as low as 1.8 % and 1.4 mrad, respectively. For a different parameter regime than the present experiment, electron beams with energy spread less than 1 % have been simulated by post acceleration after a high density gas jet [19]. In order to achieve 1 % energy spread in the simulation, the downramp had to be terminated in a plasma channel with uniform axial density immediately after the particles were trapped, such that the electrons were correctly phased in the wake and beam loading was balanced to produce even accelerating field across the bunch. In addition matched guiding was required to prevent further evolution of the laser spot size after injection. Geometrical changes to the design will be made to meet these requirements in future experiments.

Injection of electrons was investigated using the particle-in-cell modality of INF&RNO . Shown in Fig. 3 is the laser vector potential a_0 (dash-dot line), which increases to ≈ 3.5 compared with the vacuum focal value of ≈ 1.5, producing a bubble wakefield. The wake phase velocity (dashed line) is reduced in the region where the density is decreasing and the laser intensity is increasing, and trapping of particles is observed in the grey shaded region. The contribution to the phase velocity reduction by self-focusing can be determined

by comparing the wake phase velocity for vacuum $a_0 \approx 1.5$ (dashed line) with a vacuum $a_0 \approx 0.1$ (red solid line), since for the latter self-focusing can be neglected. It can be seen that self-focusing causes a significant reduction in wake phase velocity. Injection occurs over only a short propagation distance, since the wake phase velocity increases as the ramp is terminated and the laser reaches maximum intensity.

The trends observed with Δx_{f} and n_{jet} were investigated using the fluid modality of INF&RNO (described in the methods section). Figure 4 (a) shows the effect of the gas jet on the laser intensity and focal position as a function of gas jet density and laser vacuum focus. The jet causes laser pulse self-focusing, which is increased for lower Δx_{f} or higher n_{jet}. This explains the increase in charge with n_{jet} observed in Fig. 2 (g), since the laser intensity and wakefield amplitude increase, and the injection location is shifted upstream closer to the peak of the density profile. The lower charge observed in Fig. 2 (b-f) can also be understood, since n_{jet} was approximately a factor of 2 lower. Further evidence for self-focusing is shown in Fig. 5, where experimental laser spectra are shown for targets of no plasma, jet only, and jet with capillary for peak densities in the jet between $4 \times 10^{18}\,\mathrm{cm}^{-3}$ and $5.5 \times 10^{18}\,\mathrm{cm}^{-3}$. Significantly more redshifting was observed when the capillary was introduced, compared to only operating the jet, showing that a significant wake was present in the capillary. Furthermore, redshifting increased with jet density, consistent with increased laser intensity and a larger wake in the capillary. A similar trend was observed in simulations.

Self-focusing was also the dominant effect in determining energy gain, since increased self-focusing, whether it be from reducing Δx_{f} or increasing n_{jet}, reduces the focused laser spot size and makes diffraction of the laser pulse in the non-matched plasma channel more severe. This reduced the average laser intensity over the channel length and the final energy gain. The energy gain can be estimated by considering the field excited by the focused laser pulse integrated over the interaction length limited by laser diffraction, which is longer than the Rayleigh range due to nonlinear self-focusing and plasma channel guiding. Figure 4 (b) shows the energy gain $m_{\mathrm{e}}c^2\Delta\gamma$ for several Δx_{f} calculated using $\Delta\gamma \simeq \pi^2 \left[(a_0^2/2)/\sqrt{1+a_0^2/2}\right] (Z_{\mathrm{eff}}/\lambda_{\mathrm{p0}})$ [1]. Both the laser vector potential at focus a_0 and the effective acceleration length Z_{eff} were obtained from simulation. Figure 4 (b) shows qualitative agreement between the estimated diffraction-limited energy gain and the experimental measurement shown in Fig. 2. This demonstrates that the key mechanism determining the energy gain is diffraction of the laser pulse, which can be controlled by

changing injector and channel parameters. This is in contrast to previous LPA experiments employing the hydrogen-filled capillary discharge waveguide [2], where a higher density was employed and diffraction mitigated to allow acceleration to dephasing and higher energy gain.

The shot-to-shot stability of the beams is significantly better than that achieved in previous experiments. The root mean square (rms) variation in energy, charge, and pointing for consecutive shots shown in Fig. 2 (c) was 1.9 %, 45 %, and 0.57 mrad, respectively, and as shown in Fig. 2 (b-f), this high degree of stability is not limited to a narrow range of parameters. The charge stability was reduced to 6 % by small changes to the density profile, representing more than a four-fold improvement over current state-of-the-art LPAs using the more complex injection scheme of multiple laser pulses [29]. The laser beam had a Strehl ratio of ≈ 0.9 and the laser energy fluctuation was 3 %.

Deconvolving the laser energy fluctuation, which was correlated to charge fluctuation, indicates that the charge variation could be reduced to below 4 %. Injection assisted by partially ionized gas species could improve stability further since less self-focusing of the laser pulse is required. This could also be advantageous for matched guiding in the lower density structure since the focused spot size could be larger.

METHODS

Laser

Pulses from the LOASIS Ti:sapphire laser system were focused onto the gas targets by a 2 m focal length off-axis parabolic mirror to a focal spot size of $r_0 = 22\,\mu$m (Fig. 1) [2]. This corresponds to a Rayleigh range $Z_R = 1.9$ mm. For these experiments the laser energy on target was 1.4 J, corresponding to a peak intensity of $4 \times 10^{18}\,\mathrm{Wcm}^{-2}$ for a pulse length of 38 fs.

Laser and electron beam diagnostics

Laser radiation emerging from the capillary passed through the electron spectrometer and was attenuated by reflection off two optically flat wedges. The energy of each laser pulse input to the waveguide was determined by a photodiode that was calibrated to the

energy on target. The energy of pulses transmitted through the capillary was measured by loosely focusing the portion of the laser beam transmitted through the second wedge onto a pyroelectric energy meter that was cross-calibrated to the input photodiode.

The energy of electron bunches emerging from the plasma was measured by a magnetic electron spectrometer [25]. A 1.2 T magnet deflected the electrons onto phosphor screens imaged by four synchronously-triggered CCD cameras, enabling single-shot detection of electrons with energies in the range $0.01 - 0.14$ GeV and $0.17 - 1.1$ GeV. Charge was obtained from the phosphor screens, which were cross-calibrated against an integrating current transformer. This diagnostic provided charge density images of the electron beam with energy in one direction, and angle in the undispersed plane.

Capillary waveguide and embedded gas jet

The capillary employed had diameter 220 μm and length 33 mm. Hydrogen gas was flowed into the capillary via slots located 3.85 mm from each end of the capillary. Helium gas filled the injector nozzle, which was located at a distance of 1.38 mm after the entrance of the capillary. The discharge current was approximately sinusoidal, with peak current 250 A. Data was taken for the laser arrival 390 ns after the onset of the discharge, which was within a few tens of ns from the peak of the discharge. The on-axis electron density and matched spot of the waveguide were calculated from the backing pressure as described in Ref. 27. The matched spot of the waveguide was between 45 and 50 μm.

The density profile for the jet injector was measured with a Michelson interferometer with the probe beam shown in Fig. 1 (c). The injector experiments employed different gases (hydrogen, helium, and a gas mix of 1% nitrogen balance helium), at plasma densities between $4 \times 10^{18}\,\mathrm{cm}^{-3}$ and $14 \times 10^{18}\,\mathrm{cm}^{-3}$. The plasma length (FWHM) was scanned between 0.55 mm and 1.3 mm, and the focal location 3 mm before to 4 mm after the jet center.

Transverse optical access to the jet was not available for the jet embedded into the capillary. In order to obtain the density in this case neutral gas interferometry with a wavefront sensor was performed on a similar gas jet without capillary and found to be within 20 % of simulations done using a commercial fluid dynamics code. Simulation of the jet embedded in the capillary showed the density profile not to be significantly affected

and gas did not flow into the capillary section. The peak density in the simulation was $n_{\rm jet} = 13 \times 10^{18}\,{\rm cm}^{-3}$ for the conditions of Fig. 2 (a), but this is an upper limit since after the discharge is struck, Ohmic heating causes expansion of the gas and a reduction in density. An estimate of the decrease in density due to Ohmic heating was obtained by comparing laser energy depletion data of the jet alone with the jet embedded into the capillary. energy depletion for jet and capillary should be equal to or greater than that for the jet alone for the same jet density. With this assumption, an upper limit to the density is $n_{\rm jet} = 1 \times 10^{19}\,{\rm cm}^{-3}$. By lowering the capillary density, energy depletion decreased. By assuming the minimum observed energy depletion is close to the value of the jet alone, a better estimate for the conditions of Fig. 2 (a) is $n_{\rm jet} \approx 7 \times 10^{18}\,{\rm cm}^{-3}$. The initial gas density was reduced by 2, and this correction was applied for all data. Shot-to-shot stability density from the jet was measured to be at least as low as 4 % which was the measurement error of the interferometric technique.

INF&RNO

Calculations of the laser-plasma interaction (laser and wakefield evolution, energy gain for electrons) are carried out with the computational framework INF&RNO (INtegrated Fluid & paRticle simulatioN cOde). INF&RNO is a 2D cylindrical ($r - z$) code that adopts an envelope model for the laser pulse and makes use of the ponderomotive force approximation to describe the interaction of the laser pulse with the plasma [1]. The plasma can be modeled using either a fluid or a fully kinetic description, the latter being realized through the Particle-In-Cell (PIC) approach. Both PIC and fluid modalities are integrated in the same framework allowing for staged simulations (*e.g.*, PIC-mode for injection and fluid-mode for acceleration). The electromagnetic field associated with the plasma wake and the laser envelope are managed using a finite difference approach. All the fields are discretized onto a grid and spatial derivatives in the evolution equations are computed with second order upwind (in the longitudinal direction) or centered (in the transverse direction) finite differences schemes. Temporal update of the wakefield is carried out using a 2^{nd} or 4^{th} order Runge-Kutta integrator, while a 2^{nd} order Crank-Nicolson method is adopted for the laser envelope. For the plasma description in the fluid modality, additional fields for the density and momentum density are included. In the PIC modality the plasma phase

space distribution is represented using numerical particles which are advanced solving the relativistic equations of motion with a 4^{th} order Runge-Kutta integrator. Quadratic shape functions are used for force interpolation and charge/current deposition onto the grid. Non-uniform/adaptive particle sampling is adopted to minimize statistical noise and increase accuracy within the dynamically interesting zones without greatly increasing the overall number of simulated particles. A Boosted-Lorentz-Frame modeling capability for the fluid modality is also available allowing for a significant speedup in the calculations. Compared to standard simulation tools INF&RNO allows for a reduction of many orders of magnitude in computational time, while retaining physical fidelity.

ACKNOWLEDGMENTS

The authors would like to thank E. Cormier-Michel, M. Chen, J. Mefford, N. Matlis and G. Plateau for useful discussions. We appreciate contributions from D. Syversrud, Z. Eisentraut, K. Sihler, and N. Ybarrolaza. This work was supported by the Director, Office of Science, Office of High Energy Physics, of the U.S. Department of Energy under Contract No. DE-AC02-05CH11231, by the National Science Foundation under Grants PHY-0935197 and PHY-0917687, and by the Defense Advanced Research Projects Agency (DARPA).

AUTHOR CONTRIBUTIONS

A.J.G. worked on the design and execution of the experiments, analyzed the data, and was the primary author of the paper. W.P.L. conceived of and supervised the project. C.L fabricated the targets and performed the neutral gas fluid simulations. K.N. analyzed electron beam images. C.B. performed the simulations of the laser-plasma interactions. E.E., C.G.R.G., C.B, and C.B.S. contributed to the understanding of experimental data, including the formulation of the theory of phase velocity control via self-focusing. C.T. worked on laser systems. The team for the experiments employing the jet embedded into the capillary included K.N., C.L., D.P., and A.J.G.. The experimental team for the gas jet experiments included K.N., C.L., T.S., J.O., J.V.T., S.S., and A.J.G..

ADDITIONAL INFORMATION

The authors declare no competing financial interests.

---

* Currently at Physical Sciences Inc., 6652 Owens Dr., Pleasanton, CA, 94588

† Currently at University of Hamburg and Deutsches Elektronen-Synchrotron (DESY), D-22607 Hamburg, Germany

[1] Esarey, E., Schroeder, C. B. & Leemans, W. P. Physics of laser-driven plasma-based electron accelerators. *Rev. Mod. Phys.* **81**, 1229–1285 (2009).

[2] Leemans, W. P. *et al.* Gev electron beams from a centimetre-scale accelerator. *Nature Phys.* **2**, 696–699 (2006).

[3] Leemans, W. P. *et al.* Observation of terahertz emission from a laser-plasma accelerated electron bunch crossing a plasma-vacuum boundary. *Phys. Rev. Lett.* **91**, 074802 (2003).

[4] Rousse, A. *et al.* Production of a kev x-ray beam from synchrotron radiation in relativistic laser-plasma interaction. *Phys. Rev. Lett.* **93**, 135005 (2004).

[5] Fuchs, M. *et al.* Laser-driven soft-x-ray undulator source. *Nature Phys.* **5**, 826–829 (2009).

[6] Leemans, W. P. & Esarey, E. Laser-driven plasma-wave electron accelerators. *Phys. Today* **62**, 44–49 (2009).

[7] Schroeder, C. B., Esarey, E., Geddes, C. G. R., Benedetti, C. & Leemans, W. P. Physics considerations for laser-plasma linear colliders. *Phys. Rev. ST Accel. Beams* **13**, 101301 (2010).

[8] Mangles, S. P. D. *et al.* Monoenergetic beams of relativistic electrons from intense laser-plasma interactions. *Nature* **431**, 535–538 (2004).

[9] Geddes, C. G. R. *et al.* High-quality electron beams from a laser wakefield accelerator using plasma-channel guiding. *Nature* **431**, 538–541 (2004).

[10] Faure, J. *et al.* A laser-plasma accelerator producing monoenergetic electron beams. *Nature* **431**, 541–544 (2004).

[11] Umstadter, D., Kim, J. K. & Dodd, E. Laser injection of ultrashort electron pulses into wakefield plasma waves. *Phys. Rev. Lett.* **76**, 2073–2076 (1996).

[12] Esarey, E., Hubbard, R. F., Leemans, W. P., Ting, A. & Sprangle, P. Electron injection into plasma wake fields by colliding laser pulses. *Phys. Rev. Lett.* **79**, 2682–2685 (1997).

[13] Ting, A., Kaganovich, D., Gordon, D. F., Hubbard, R. F. & Sprangle, P. Generation and measurements of high energy injection electrons from the high density laser ionization and ponderomotive acceleration. *Phys. Plasmas* **12**, 010701 (2005).

[14] Faure, J. *et al.* Controlled injection and acceleration of electrons in plasma wakefields by colliding laser pulses. *Nature* **444**, 737–739 (2006).

[15] Chen, M., Sheng, Z. M., Ma, Y. Y. & Zhang, J. Electron injection and trapping in a laser wakefield by field ionization to high-charge states of gases. *J. Appl. Phys.* **99**, 056109 (2006).

[16] Pak, A. *et al.* Injection and trapping of tunnel-ionized electrons into laser-produced wakes. *Phys. Rev. Lett.* **104**, 025003 (2010).

[17] McGuffey, C. *et al.* Ionization induced trapping in a laser wakefield accelerator. *Phys. Rev. Lett.* **104**, 025004 (2010).

[18] Bulanov, S., Naumova, N., Pegoraro, F. & Sakai, J. Particle injection into the wave acceleration phase due to nonlinear wake wave breaking. *Phys. Rev. E* **58**, R5257–R5260 (1998).

[19] Geddes, C. G. R. *et al.* Plasma-density-gradient injection of low absolute-momentum-spread electron bunches. *Phys. Rev. Lett.* **100**, 215004 (2008).

[20] Schmid, K. *et al.* Density-transition based electron injector for laser driven wakefield accelerators. *Phys. Rev. ST Accel. Beams* **13**, 091301 (2010).

[21] Faure, J., Rechatin, C., Lundh, O., Ammoura, L. & Malka, V. Injection and acceleration of quasimonoenergetic relativistic electron beams using density gradients at the edges of a plasma channel. *Phys. Plasmas* **17**, 083107 (2010).

[22] Reitsma, A. J. W. *et al.* Simulation of electron postacceleration in a two-stage laser wakefield accelerator. *Phys. Rev. ST Accel. Beams* **5**, 051301 (2002).

[23] Tomassini, P. *et al.* Production of high-quality electron beams in numerical experiments of laser wakefield acceleration with longitudinal wave breaking. *Phys. Rev. ST Accel. Beams* **6**, 121301 (2003).

[24] Brantov, A. V. *et al.* Controlled electron injection into the wake wave using plasma density inhomogeneity. *Phys. Plasmas* **15**, 073111 (2008).

[25] Nakamura, K. *et al.* Broadband single-shot electron spectrometer for gev-class laser-plasma-based accelerators. *Rev. Sci. Instrum.* **79**, 053301 (2008).

[26] Spence, D. J. & Hooker, S. M. Investigation of a hydrogen plasma waveguide. *Phys. Rev. E* **63**, 015401 (2001).

[27] Gonsalves, A. J., Rowlands-Rees, T. P., Broks, B. H. P., van der Mullen, J. J. A. M. & Hooker, S. M. Transverse interferometry of a hydrogen-filled capillary discharge waveguide. *Phys. Rev. Lett.* **98**, 025002 (2007).

[28] Rowlands-Rees, T. P. *et al.* Laser-driven acceleration of electrons in a partially ionized plasma channel. *Phys. Rev. Lett.* **100**, 105005 (2008).

[29] Rechatin, C. *et al.* Quasi-monoenergetic electron beams produced by colliding cross-polarized laser pulses in underdense plasmas. *New J. Phys.* **11**, 013011 (2009).